
Article:
García, Andrea Muñoz, Budarin, Vitaliy L., Zhou, Yixin et al. (9 more authors) (2017) Monolithic mesoporous graphitic composites as super capacitors : From Starbons to Starenes®. Journal of Materials Chemistry A. pp. 1119-1127. ISSN 2050-7496

https://doi.org/10.1039/c7ta09338a

Journal of Materials Chemistry A

PAPER

Monolithic mesoporous graphitic composites as super capacitors: from Starbons to Starenes®†

Cite this: DOI: 10.1039/c7ta09338a

Andrea Muñoz García,[a] Vitaliy L. Budarin,[a] Yixin Zhou,[a] Mario De bruyn,[a] Andrew J. Hunt,[ab] Leonardo Lari,[c] Vlado K. Lazarov,[c] Horacio J. Salavagione,[d] Enrique Morales,[d] Gary J. Ellis,[d] James H. Clark[a] and Peter S. Shuttleworth*[d]

Received 23rd October 2017
Accepted 16th December 2017

DOI: 10.1039/c7ta09338a

rsc.li/materials-a

In this study, we present a new class of monolithic mesoporous carbonaceous materials produced *via* the carbonisation of a mesoporous starch aerogel highly doped with graphite. Consecutive ball milling, microwave assisted gelation and carbonization treatment produced a high concentration of dispersed graphite. These treatments induce a strong interaction between the graphite particles and the developing carbonaceous matrix, including partial delamination of graphite and the merging of the nanoflakes into the carbonaceous structure. From a combination of SEM and TEM it was found that the graphite particles reduced in size to 24 and 37 nm, matching the pore wall sizes of the produced materials. From XRD, ball milling and heating helped reduce the number of graphene layers by 40%, with presence within the porous starch matrix reducing this a further 13%. The high degree of graphite dispersion/incorporation induces a pronounced increase in conductivity, and excellent capacitance retention, in excess of 10 000 charge–discharge cycles, offering a cost efficient and sustainably produced alternative to activated carbon based EDLCs and importantly, the resultant monolithic structures mitigate the need for additional binders.

Introduction

The growing importance of portable electronic devices and hybrid electric vehicles in the market place are driving the demand for next-generation technological performance in the battery and capacitor sectors.[1] Batteries operate by converting chemical energy to electrical energy and provide high energy densities, but can only be charged and deliver that energy relatively slowly. In contrast, capacitors can release high amounts of energy over a relatively short time duration, and can operate at high charge and discharge rates over an almost unlimited number of cycles. This makes capacitors very attractive in energy recovery, especially for heavy duty systems.[2] However, the goal of delivering a high charge density over a long duration at economic cost has yet to be achieved. Thus, a combination of battery and capacitor technologies are needed to satisfy the growing technological demand. Electrochemical capacitors (ECs), also known as ultra- or super-capacitors go some way to meet both requirements of high power and high energy densities.[3] The main uses of ECs includes applications in solar arrays, micro energy harvesting systems, stop-start fuel saving in cars, LED devices, *etc.*[4–6] Energy storage in these devices operates *via* two types of mechanism: (i) pseudo-capacitance, where the active species experience fast and reversible redox reactions at well-defined potentials; (ii) electrical double-layer capacitance (EDLC), where electrostatic adsorption of electrolyte ions occurs on the large inner surface of the porous electrodes.[7] In the latter, by the application of a current, polarization at the EDLC electrode/electrolyte interface occurs generating a charged double layer. The major challenges in EDLC technology are to find materials with high conductivity, large surface area, good adsorption capability and chemical stability, and new sustainable methodologies that are both cheap and robust are vital for advancement within this sector.[8]

When compared to materials such as conducting polymers or metal organic frameworks (MOFs) *etc.*,[9] porous activated carbons are extensively used as electrodes in EDLC applications, mainly due to their relatively lower cost. They also possess high specific surface areas, good thermal stabilities over a wide range of temperatures, chemical stability in both acidic and basic media, and are easily polarizable with the possibility to introduce heteroatoms, and hence, a pseudo-capacitance element.[10] However, when using these types of materials a number of obstacles exist, such as microporosity and the need to use an inert non-conductive polymeric binder in order to prepare the

[a]Department of Chemistry, University of York, Heslington, York, YO10 5DD, UK
[b]Department of Chemistry, Faculty of Science, Khon Kaen University, Khon Kaen, Thailand 40002
[c]York JEOL Nanocentre, University of York, Helix House, Science Park, Heslington, York, YO10 5BR, UK
[d]Departamento de Física de Polímeros, Elastómeros y Aplicaciones Energéticas, Instituto de Ciencia y Tecnología de Polímeros, CSIC, c/Juan de la Cierva, 3, 28006 Madrid, Spain. E-mail: peter@ictp.csic.es

† Electronic supplementary information (ESI) available. See DOI: 10.1039/c7ta09338a

electrodes, which results in a reduction in content of the final active component and its conductivity.[10]

The problem of microporosity could be alleviated by employing hierarchical porous carbonaceous materials with a high percentage of mesopores that display: (a) ample charge storage sites due to their high surface areas (a characteristic mainly linked to the presence of micropores), (b) interconnected mesopores, (important to facilitate electrolyte migration), (c) large meso/macro-pore volume (that allow the inclusion of high capacitance guest materials), and (d) nanometer sized walls (that provide a significant enhancement of the areal capacitance).[11]

To date, few methods exist to produce carbons with high mesopore content, and those known are typically challenging and expensive to undertake,[7,12] as is the case of the only current industrial production method that is based on the use of a mesoporous silica porous template.[13] In addition, this method uses hazardous and non-sustainable high amounts of HF, or NaOH, needed to etch away the redundant silica template.[14] Hydrothermal depolymerisation and carbonisation presents an interesting alternative to produce porous carbonaceous materials, with the choice of soft, and/or hard templates, although still requiring templates.[15,16] Recently, a template-free method to synthesize mesoporous carbon has been developed, where the mesoporous structure is created during gelation and retrogradation of a helical forming polysaccharide precursor.[17,18] Crucial to this is the removal of the added water after retrogradation, *via* solvent exchange,[19] $scCO_2$ or freeze drying.[20] The obtained expanded materials are then carbonized to various temperatures in order to determine their final composition, and are trademarked as Starbon®. A particularly interesting aspect of these materials is that they can be shaped into monolithic forms, including binder-free electrodes that demonstrate considerable advantages over those synthesised from powders. Moreover, Starbon® materials do not require templates or subsequent template removal, and their production is a more efficient and sustainable process.

However, electrical conductivity for EDLC type applications of carbon materials has been shown to be highly important.[21] One method to improve conductivity is to prepare the materials at higher temperatures; for activated carbons it has been shown to reduce the energy band gap sufficiently and change the turbostratic carbon form from semi-conductive to conductive, but they need to be heated to temperatures between 1200–2000 °C.[22] This treatment requires a lot of energy, leads to significant costs from both the energy requirements and product mass loss, and can significantly alter the pore structure. From percolation theories, conductivity increases sharply when the volume fraction of a conductive phase in binary mixtures reaches a critical amount. The addition of graphite a ready available, cheap and abundant source of conductive carbon would rectify these problems.

Herein we report on the synthesis of a novel mesoporous carbon–graphite composite monolith with enhanced stability and conductivity, denominated Starene®, and demonstrate its use as a supercapacitor electrode. Through the combination of electron microscopy and statistical analysis we show that the improved conductivity and EDLC properties of the composite originates from a graphite rod stacking mechanism facilitated by polysaccharide interaction with the graphite nanoparticles.

Experimental

Materials preparation

Graphite (0, 5, 10 and 20% w/w) was added to Hylon VII corn starch and subsequently ball milled in a Retsch Planetary Ball Mill PM 100, with a 250 mL capacity containing stainless steel balls of 10 mm diameter. Samples were milled in three cycles of 10 min with a 15 min interval between each run at a rate of 400 rpm. The resulting product was mixed with water in a ratio 1 : 4 and subsequently heated at 140 °C (90 W) for 10 min in a CEM II Discover microwave. The material was then poured into a cylindrical mould and retrograded at 5 °C for 48 h to yield a porous monolith gel block. This was subjected to three solvent exchanges with *tert*-butanol (*t*BA) and then frozen using liquid nitrogen (10 min) and subsequently freeze-dried (24 h). The dried monolith was then added to a jar containing acetone doped with a catalytic amount of *p*-toluenesulfonic acid (0.1 mmol *p*-TSA/1 g of Hylon VII). A vial containing a magnetic stirrer was also immersed in the solvent to facilitate agitation of the solvent around the polysaccharide monolith without damaging it. The magnetic stirrer was set at 100 rpm and left for 1 hour, after which the sample was removed and dried in a vacuum oven set at 50 °C for 2 hours. Finally, samples were pyrolysed under vacuum at 800 °C in a Barnstead Thermolyne 6000 Furnace, to yield the samples Starbon®800 (0% w/w graphite added) and Starene®800_5, Starene®800_10 and Starene®800_20, with 5, 10 and 20% w/w graphite added, respectively.

Characterisation

SEM micrographs were obtained using an ultra-high field-emission scanning electron microscopy (FESEM) (SU8000, Hitachi Co., Japan). Nitrogen physisorption was carried out using an ASAP 2020 from Micrometrics, with measurements performed at 77 K. Pre-carbonised (~80 mg) and carbonised (~40 mg) samples were degassed under vacuum at 40 °C and 130 °C respectively for 6 h prior to analysis. The Brunauer–Emmett–Teller (BET) methodology was used to determine the surface area, with a minimum of 5 data points used over a relative pressure range of (P/P_0) 0.05–0.30, maintaining a linear relationship and an $R^2 \geq 0.995$. Mesoporous volume and the pore size distributions were calculated by applying the Barret–Joyner–Halenda (BJH) equation to the adsorption branch of the N_2 sorption isotherms. *t*-plot analysis was employed using the fitted layer thickness range from 0.32 to 0.5 nm. Dubinin–Astahov (D–A), where a linear fit of ~10 points were obtained, typically over the relative pressure (P/P_0) range 0.00015–0.12, and the Dollimore–Heal and DFT models were applied over the full P/P_0 range.

Conductivity measurements were carried using a computer controlled Hewlett-Packard 6614C dc power supply and two Hewlett-Packard 34401A multimeters, with the samples set in

a two-probe configuration. The amplitude of the applied dc signal was 1 V and six measurements were made for each sample over 1.5 h. TGA was carried out on 10 mg samples using a Netzsch STA 409 C/3/F under a 100 mL min^{-1} constant N_2 flow and a heating rate of 1 °C min^{-1}. The theoretical concentration of graphite after pyrolysis was calculated from the values of mass residue recorded by TGA, minus the equivalent mass residue of the carbonised material without graphite added. To identify the temperature regions in which significant mass loss occurred during heating, a first order derivate was applied to the TGA curves. To calculate the experimental mass of graphite, the reference curve was multiplied by the percentage of amorphous carbon, to obtain comparable traces. The residue of the reference material was subtracted from the residue of the composite traces.

X-ray photoelectron microscopy (XPS) was carried out at the NEXUS National EPSRC XPS Users' Service, Newcastle University (UK) on the K-Alpha™ (Thermo Scientific™, East Grinstead, UK) spectrometer utilising a micro-focused monochromatic Al Kα source (1486.6 eV). For the high resolution spectra of the elements of interest a pass energy of 40 eV and a step size of 0.1 eV was used. Samples were mounted on microscope glass covers using double-sided tape. Data analysis was performed using CasaXPS software and the C 1s binding energy was calibrated to 284.4 eV, with a precision of ±0.2 eV. Deconvolution of the experimental curves was carried out using a combination of Lorentz (30%) and Gaussian (70%) after eliminating the S-shaped baseline to obtain the intensities of the different chemical contributions.[23]

TEM micrograph images were recorded using a Tecnai 12 BioTwin at 120 kV. Electron images and diffraction patterns where obtained using a JEOL 2010F operating at 200 kV. Electron energy loss spectroscopy studies (EELS) were undertaken in transmission mode using a 200 kV JEOL 2200FS, probe and image aberration corrected, and equipped with an in-column (Omega) energy filter. Samples were suspended in ethanol and deposited onto carbon grids *via* solvent evaporation.

Electrochemical analysis

Supercapacitor electrodes were processed as cylindrical pellets (10 mm diameter, thickness < 1 mm). Symmetrical supercapacitors were assembled in Swagelok™-type cells, using a glassy microfibre paper (Whatman 934AH) separator and a 2 M H_2SO_4 aqueous solution as electrolyte. Two stainless steel (A20 alloy) rods acted as current collectors. Room temperature cyclic voltammetry, galvanostatic charge–discharge and impedance spectroscopy tests were performed by using a Solartron 1480 potentiostat/galvanostat instrument coupled to a Solartron 1255B frequency response analyser, in the potential range 0–1 V. Prior to the analysis, samples were dried overnight at 100 °C under vacuum.

The electrochemical behaviour in terms of specific capacitance and cyclability of the selected materials were tested. The specific capacitance of the material was calculated from the discharge run of the cyclic voltammograms using the following formula:

$$C = \frac{\left(\int I\mathrm{d}V\right) \times 2}{\Delta V m v}$$

where C is the specific capacitance, expressed in F g^{-1}, I is the current, in A, V is the potential applied, ΔV is the voltage window, expressed in V, v is the scan rate, in V s^{-1} and m is the mass of the active material of a single electrode (based on the theoretical concentration of graphite determined from TGA) in grams, *i.e.* only the mass of the carbonised polysaccharide.

The cycling performance of the symmetric electrochemical capacitors was evaluated using galvanostatic charge/discharge over 10 000 cycles at a constant current density of 25 mA, using the relationship:

$$(C_n/C_1) \times 100$$

where C_n is the specific capacitance of the nth cycle (F g^{-1}) and C_1 the specific capacitance of the first cycle. Values of C_n and C_1 were calculated from the galvanostatic discharge process by using the expression:

$$C_{sp} = \frac{2I \times t_d}{\Delta V 2 m_{electrode}}$$

where I is the current applied in A, t_d is the discharge time in seconds, $\Delta V2$ is the voltage range in which the discharge occurs, and $m_{electrode}$ is the active mass of a single electrode (based on the theoretical concentration of graphite) expressed in grams.

Results and discussion

Cylindrical monolithic mesoporous carbon with a diameter of 10 mm and a density of 0.34 g cm^{-3} was prepared (Fig. 1a) and sections of <1 mm thickness cut (Fig. 1b) and used as electrodes. These were assembled symmetrically into a two-electrode Swagelok™-type EDLC cell, using a glassy microfibre paper membrane as a separator, and 2 N H_2SO_4 aqueous solution as the electrolyte, as shown in Fig. 1c. From cyclic voltammetry (CV) at a potential scan rate of 1 mV s^{-1}, gravimetric and volumetric (C_V) capacitances of 175 F g^{-1} and 61 F cm^{-3}, respectively, were measured for the prepared Starbon®800 material (Fig. 1d and e). The gravimetric and volumetric capacitance of the tested material falls within a range for carbons adopting aqueous electrolytes as reported in recent literature, of 45–300 F g^{-1} (25–400 F cm^{-3}).[24] However, despite the fact that single layer graphene has a predicted gravimetric capacitance of 355 F g^{-1},[25] porous carbons without high-cost nanoparticles or heteroatom addition, typically show values <220 F g^{-1} (180 F cm^{-3}).[26–28] Using a constant current galvanostatic charge/discharge technique, the stability of the Starbon®800 was assessed over 10 000 cycles at an applied current density of 25 mA cm^{-2} (Fig. 1e). It can be seen that the capacitance drops significantly (−3.5%) after the first 100 cycles and appreciably (−15%) towards the 10 000 cycles mark.

In order to improve the performance of these materials, it was hypothesized that the addition of a conductive carbon could help with the transfer of electrons, reducing the internal resistance of the electrodes and limiting the local generation of

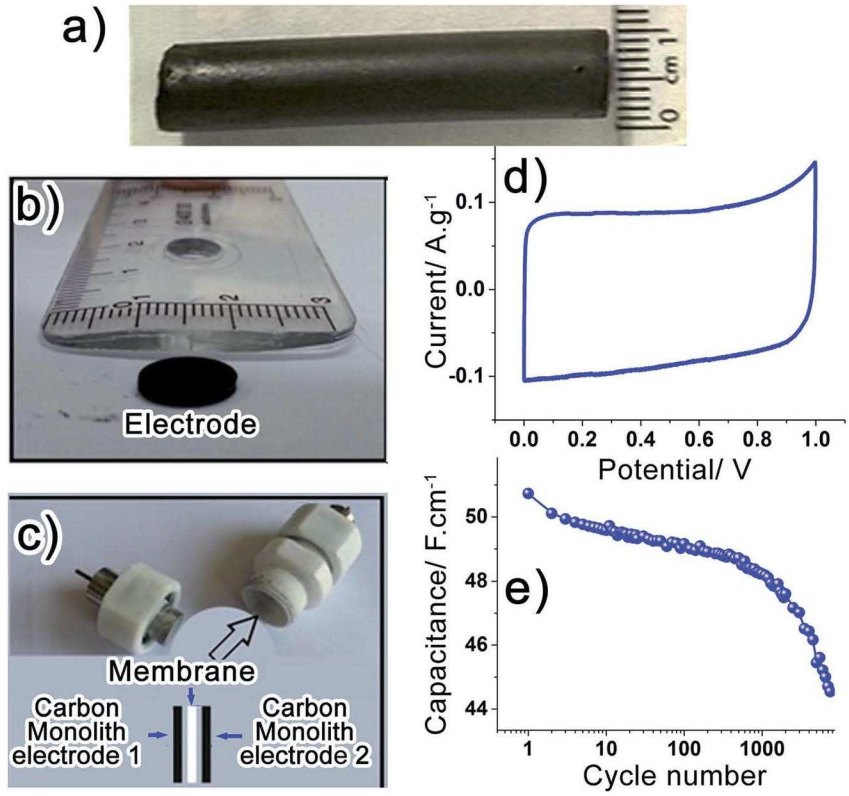

Fig. 1 Images of (a) monolith of Starbon®800; (b) a cut to size electrode; (c) electrochemical cell where the electrodes were inserted; (d) cyclic voltammetry of Starbon®800 at a scan rate of 1 mV s^{-1}; (e) capacitance retention over 10 000 cycles for Starbon®800 at an applied current density of 25 mA cm^{-2}.

heat.[29] In this respect it has recently been reported that the addition of <10% expanded graphite can increase the conductivity of starch up to 10 times.[30] Graphite was chosen as it is cheap, a good conductor and readily available.[31] Although, graphite cannot be easily dispersed in water nor in an organic solvent[32,33] various methods were tested in order that a stable dispersion within the polysaccharide could be achieved (see ESI, Fig. S1†).

Graphite introduction into the starch precursor was obtained through ball milling both components for 30 minutes to achieve a homogenous dispersion before gelation that pervaded after carbonisation. This time was found to be the minimum required to achieve a homogeneous dispersion. In fact, dry ball milling of graphite with other polysaccharides has been found to be particularly effective for its exfoliation and dispersion, and led to a lower graphite concentration required for electrical percolation compared to the thermoplastics tested such as, PMMA and polystyrene *etc.*[34] Gelation of the homogenised powder in water was carried out at 140 °C under microwave conditions. It was found that it was not possible to obtain a homogeneous gel after the addition of 20% w/w graphite, and as such trials were carried out with this material as one of the objectives was to reduce the cost of the material, and to better understand the interaction and resulting structure and physical properties of materials with a high graphite loading. The water from the gel was removed *via* lyophilisation, and the samples were subsequently carbonised up to a temperature of 800 °C.[17]

The prepared samples were assessed for porosity retention both before and after carbonisation using nitrogen sorption. From Fig. S1, S2 and Table S1, ESI† and Fig. 2a it can be observed that the isotherms for Starbon® and its graphite composites, Starenes®, are Type IV,[35] thus confirming that all the materials remained mesoporous irrespective of the amount of graphite added, up to the 20% w/w threshold. However, the pore size distributions (PSD) of these materials were strongly affected by the graphite loading, with their maximum pore diameters (PD_{MAX}) in the mesopore region varying from 22 nm for Starbon®800 to 44 nm for the material containing 20% w/w graphite (see Fig. 2b). Further evaluation of the textural parameters obtained from the BJH using Dollimore–Heal, DFT and *t*-plot methods produced similar results as shown in the Table S2.†

The conductivities of the prepared samples were determined (see Fig. 2c and Table S3†), with the maximum value observed for the sample with 20% w/w graphite, having a more than twenty-one times increase in conductivity, from 0.007 to 0.148 S cm^{-1}. From a sigmoidal fit of the data presented in Fig. 2c, a percolation threshold of $\phi_c = 4.84\%$ w/w was found. This increase in conductivity can be explained by a more than double C/O ratio for Starene®800-G20 compared to the control without graphite (see Table S4†), and an increase in the conductive routes throughout the porous network for the 10 and 20% w/w samples respectively.

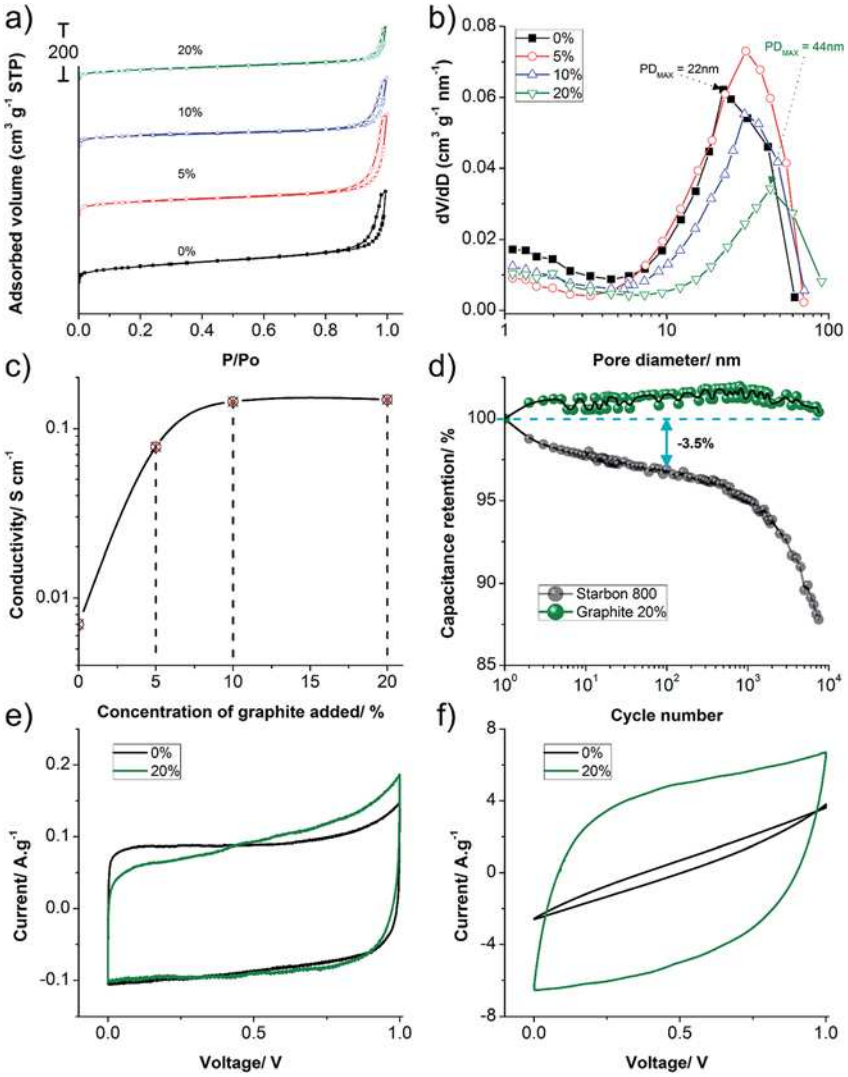

Fig. 2 (a) N_2 sorption isotherms stack plot of the porous graphite composites; (b) change in pore size distribution with increasing concentrations of added graphite; (c) conductivity as a function of added graphite, error in red; (d) relative capacitance retention over 10 000 cycles for both the standard Starbon®800 and the Starene®-G20; (e and f) cyclic voltammograms of both the Starbon®800 and the Starene®-G20 at scan rates of 1 mV s^{-1} and 100 mV s^{-1}, respectively.

Furthermore, the Starene®800-G20 monolith was shown to be highly stable as a capacitor, with a performance loss of <1% over 10 000 cycles (Fig. 2d, green line). This follows from the aforementioned argument (ref. 11) that a higher conductivity reduces the internal resistance of the electrodes and, hence, local heat generation. This is of particular importance for high surface area materials with thin pore walls, which have limited resistance to the combination of heat and aggressive dielectric media. This important result is verified by the cyclic voltammograms shown in Fig. 2e and f, where at a low scan rate the curves for the capacitors show an almost ideal rectangular shape, whereas at higher scan rates their shape deviates from ideal, and it can be seen that the poorly electrically conductive Starbon®800 sample ceases to act as a capacitor. In addition, the C_V, which has been described as a more accurate method to report capacitance from an application perspective, can be seen to increase by 39% (85 F cm^{-3}) for Starene®800-G20 compared to the standard, suggesting that the composite material can store more charge per unit volume.[36] This is related to the almost 50% increase in the density of the material and, consequently, in its pore structure packing (Fig. S3†). Changes in the C/O surface chemistries described earlier will also induce a faster polarisation of the surface – electrolyte, improving its capacitance. Further, due to a slightly lower surface area and larger pore structure the resulting surface will be more planar at the average charge separation distance, which has been reported to lead to improved areal capacitances.[25] From Fig. S4† of the rate capability, it can also be seen that the diffusion into the pore structure of the Starene®800-G20 monolith is less hindered at high current densities compared to the material without graphite.

In order to better understand the electrochemical performances of the electrodes, electrochemical impedance spectroscopy was employed (EIS). All the electrodes were measured

in the frequency range of 500 kHz to 50 mHz at an amplitude of 10 mV. From the Nyquist plots shown in Fig. S5,† a depressed semi-circle in the high frequency range can be observed that corresponds to the bulk RC response, and at low frequencies there is a spike related to charging. The bulk RC response for the Starbon®800 capacitor is larger than that of the Starene®800_20% verifying that the graphite is helping reduce the electrical resistance of the electrode. At low frequencies the electrodes with 0 and 20% w/w graphite show a 14° to 10° deviation respectively from that of 90° identified with pure capacitance. These slight differences have been related diffusion resistivity of the electrolyte within the pore, and for carbon materials due to their wide pore size distributions.[37]

To further understand the nature of the enhanced performance of the Starene® materials, structural characterization was performed using SEM and TEM, see Fig. 3.

The low-resolution SEM images demonstrate the dramatic transformation of the heterogeneous graphite-starch system (Starene®200-G20) that contains up to 10 μm diameter large graphite flakes, to the more uniform fibrous structured material carbonised at 800 °C (Starene®800-G20), see Fig. 3a and b. Interestingly, the high-resolution SEM demonstrates that in the presence of graphite the original Starbon®800 fibrous structure (Fig. 3c) aggregates to a network with a more open structure and thicker walls (see Fig. 3d and S6–S8 (ESI)†). This data is in good agreement with that related to the increase in the pore diameter of the materials in the presence of graphite (see Fig. 2b). Statistical analysis of the diameter of the individual fibres based on these images shows that no difference in the fibre widths can be discerned for the samples with 0, 5 and 20% graphite, with two peaks centred around 25 and 35 nm (Fig. 3f, g and S7 ESI†). Intriguingly, these dimensions correspond well with the

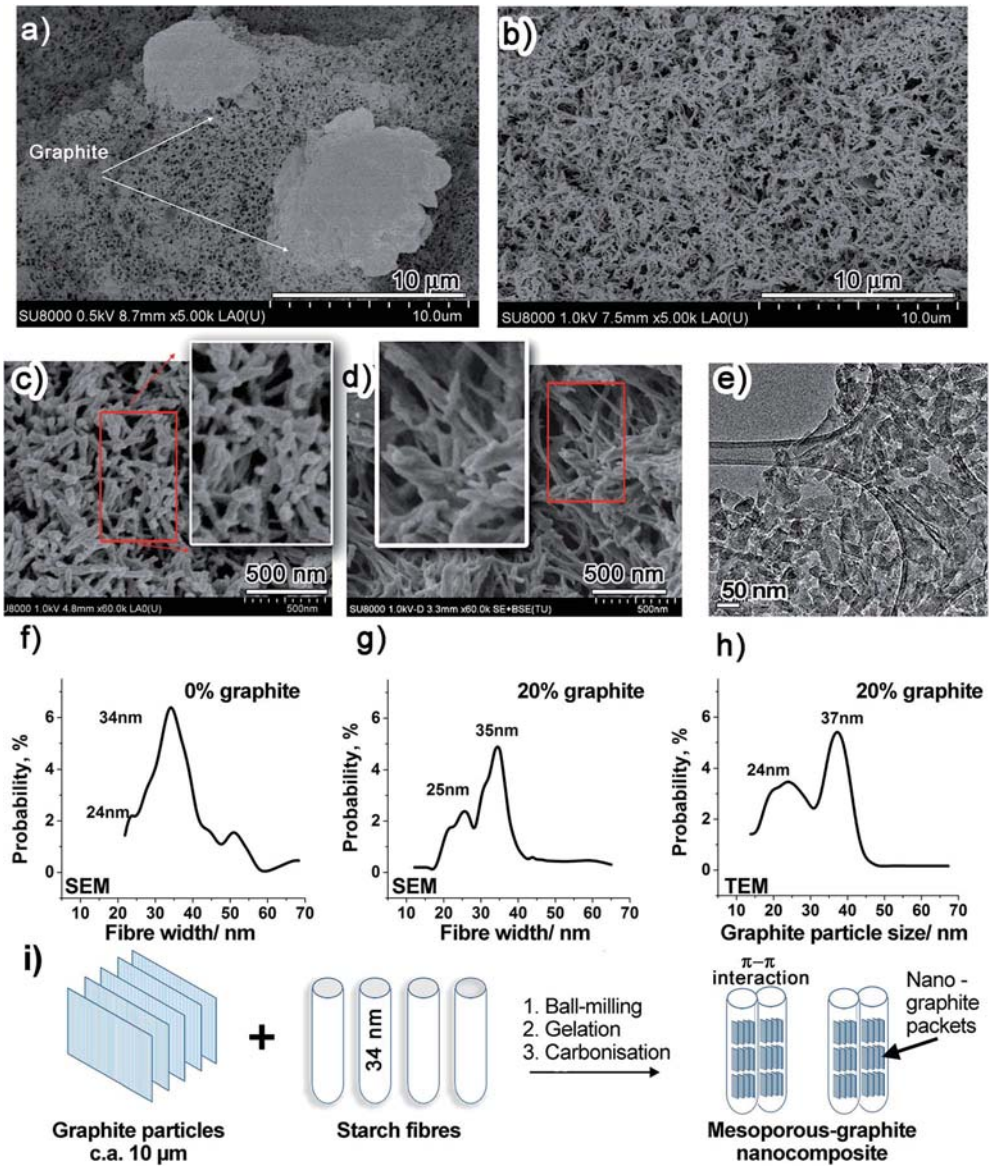

Fig. 3 (a) SEM of Starene®200_20%; (b) SEM of Starene®800_20% (comparative to d); (c) SEM of Starbon®800; (d) SEM of Starene®800_20%; (e) TEM of Starene®800_20%; (f, g and h) are particle size distributions of the images shown in (c, d and e) respectively.

graphite nano-particle sizes (24 and 37 nm) found for Starene®800-G20 using HR-TEM (Fig. 3d and h, S7 ESI†), suggesting that there is an underlying mechanism occurring of incorporation and size restriction of the graphite particles to that of the fibre width.

Initial co-milling of the graphite with the starch could lead to some chemical modification of the carbon apart from just its exfoliation, as demonstrated Sun *et al.*[34] They showed using FTIR that co-milling graphite with cellulose after 24 h amongst other polysaccharides induces OH and COOH functionalities on the graphite surface. The ball milling time used here was much lower than that described, but does suggest that there is possibility of increased compatibility between the two components. Separation of the two components does not occur during carbonisation as initially the graphite particles are unable to agglomerate because the starch is solid. At higher temperatures (approx. 300 °C) the starch either passes *via* an acid catalysed decomposition route from the polysaccharide to the carbon or *via* a highly viscous molten phase,[17,38] again preventing phase separation and graphite particle agglomeration.[39] With increasing temperature the two phases become chemically similar resulting in very good compatibility and a strong interphase.

The reduction in graphite particle size during the carbonization could be attributed to the aggressive volatiles (*e.g.* organic and sulphuric acids, CO, CO_2) produced during

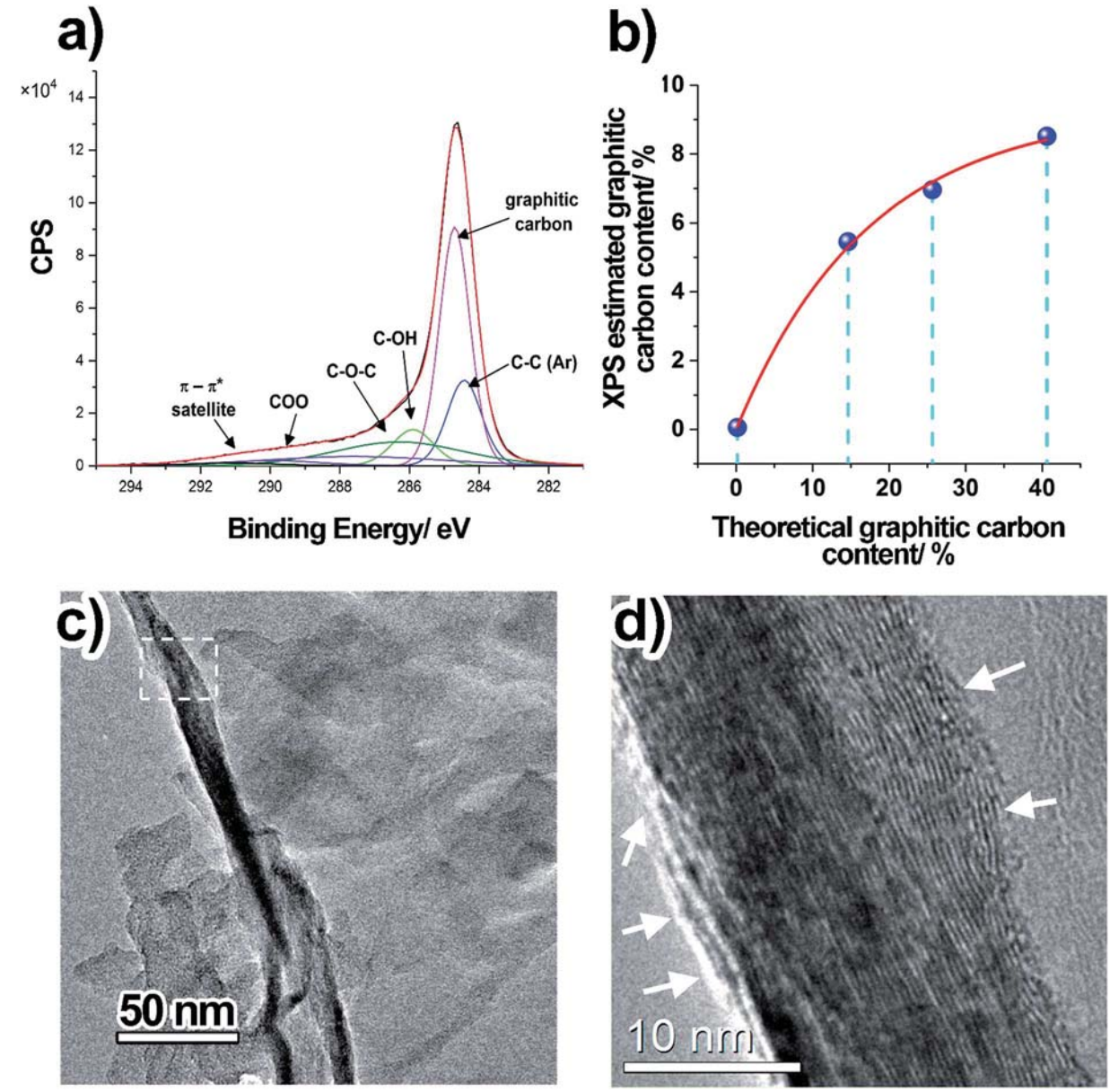

Fig. 4 (a) High-resolution XPS spectra in the C1s BE region of Starbon®800 (for Starene®800_20% see Fig. S11, ESI†); (b) XPS calculated graphitic carbon content *versus* the theoretical carbon content derived from the TGA mass loss. (c) Bright field STEM of Starene®800_20% showing graphite flakes and amorphous carbon; (d) STEM bright field from the dashed box inset in (c) showing the stacking of graphene layers as well as amorphous carbon (indicated by white arrows) surrounding the flake.

pyrolysis, as well as contact with the oxygen rich polymer molecules that become soft/molten and highly oxidative at high temperatures.[40] The loss of graphite during the carbonization process was verified using a combination of TGA and XPS with the latter revealing a pronounced discrepancy between the theoretical amount of graphitic carbon and that measured using the methodology of Desimoni *et al.*[41] (see Fig. 4a and b, and ESI, Fig. S9 and S11†).

Using TGA, a comparison of the thermal behaviour of the mesoporous starch monolith and the 20% graphite nanocomposite was carried out (see ESI, Fig. S9†). It was found that the degree of decomposition of the starch–graphite composite is substantially lower than the original starch, which could be explained by the presence of the graphite particles retarding the decomposition process.[30] To better understand the thermal events occurring, the TGA data was normalized to the actual starch content of the materials, and the normalized dTG's of these materials analyzed (see ESI, Fig. S10a and b†). It can be seen that the pyrolysis rate for these two samples is different: at low temperatures (<250 °C) graphite reduces the rate of starch decomposition, whilst at high temperatures it is equal or higher than that of the original starch material (see ESI, Fig. S10b†). Interestingly, the peak maxima of the rate differences (~270, 400, 600, and 700 °C) correspond well with the reported molecular transitions that take place during mesoporous starch decomposition.[38] Furthermore, from the SEM data the large agglomerated graphite particles that are present within the sample prepared at 200 °C are rarely seen within the sample prepared at 800 °C, further corroborating the proposed mechanism of breakdown and loss of the majority of the non-incorporated graphite.

The influence of carbonization to 800 °C was also evaluated using XRD for graphite and the prepared mesoporous carbon/graphite composites, see Table S5, ESI.† In the case of pure graphite, it was found that the crystal size decreased from 45 nm (~134 graphite layers) to 33 nm (~99 graphite layers) upon ball-milling with starch (20% w/w graphite). After heating to 800 °C the crystal size was further reduced to 27 nm (~80 graphitic layers). In comparison, the composite prepared with 5% w/w graphite, which from the SEM analysis presented virtually no evidence of large graphite particles with the majority of the nano-graphite incorporated within the carbonised starch structure, has a crystal size of 21 nm (~62 graphite layers). With increasing graphite concentration and greater presence of larger graphite particles not incorporated within the starch structure this value increases to 24 and 27 nm (72 and 74 graphite layers) for the 10 and 20% w/w samples respectively. All these values are less than those for the standard treated materials without gelation, again suggesting incorporation and loss of excess graphite. The effect of the ball-milling process on the graphite/polysaccharide interactions before pyrolysis should also be considered. As noted earlier the surface chemistry of graphitic materials can change by mechanical treatments like ball-milling, though treatments times required are much higher than that used in this study.[34] However, ball-milling does break the graphite sheets (see Fig. S12, ESI† and subsequent Raman discussion), increasing the quantity of the edge planes, which, unlike the inert basal planes present specific chemical reactivity and electronic properties that could generate particular interactions with the heated polysaccharide.[42,43] Further evidence of the high degree of graphite dispersion and the intimate interaction between the graphite nano-flakes and the polysaccharide derived mesoporous carbon medium came from studies using HTEM in combination with electron diffraction and electron energy loss spectroscopy (EELS).

The bright field STEM imaging shown in Fig. 4c and d of a sample initially prepared with 5% graphite, shows regions containing both an amorphous porous carbonaceous material and graphite nano-flakes. The high-resolution image (Fig. 4d) shows the (002) atomic planes of the graphitic flake with a thickness less than 20 nm, corresponding to approximately 50 graphitic layers. Although the graphite and the initial carbonaceous matrix are expected to be hydrophobic and hydrophilic respectively, a good connection between the two components is found, as indicated by the arrows in Fig. 4d where a thin layer of amorphous carbon down to 1 nm in thickness can be seen at the graphite edges. The crystalline component of the sample illustrated by the BF-TEM is also confirmed by the electron diffraction and Dark Field TEM as shown in Fig. S12, ESI.†

The graphitic nature of the flakes was also investigated using EELS (see Fig. S13†). The π^* and σ^* peaks corresponding to the C molecular orbitals characteristic for graphitic flakes are clearly observed in comparison[44] to the C K-edge characteristic of the amorphous carbon. Both the EELS spectra and diffraction studies show that the materials processing does not alter the crystalline nature of the graphite at the nanoscale, and hence, its conductive properties. In addition, it shows to be intimately mixed with the porous carbonaceous matrix, aiding the electrical percolation of the system.

Conclusion

In this study, we present Starene® a new class of monolithic mesoporous carbonaceous material that present good surface area and conductivity, resulting in a very stable capacitor material. To this end a technique was developed to disperse graphite in a carbonaceous material. The increased graphite dispersion is shown to be the result of consecutive ball milling, microwave assisted gelation and carbonization treatment. Furthermore, throughout these treatments a strong interaction between the graphite particles and the underlying, developing, carbonaceous material is forged, partially delaminating and reducing the size of the graphite and even merging the flakes into the carbonaceous structure. The high degree of graphite dispersion/incorporation lies at the basis of a pronounced increased conductivity, a factor essential for good long-term capacitance use, as well as on its chemical and mechanical stability. The material with 20% w/w graphite added was found to display throughout the galvanostatic charge–discharge tests <1% reduction in capacitance over 10 000 cycles in comparison to the standard that lost approx. 15% capacitance. This was related to the higher conductivity reducing the internal resistance of the electrodes. The high added concentration of graphite incorporation and use of bio-derived starting materials are also important to reduce the cost of the electrodes, whilst maintaining their credentials as a sustainable alternative electrode material.

Conflicts of interest

Acknowledgements

The authors would like to thank the ICTP-CSIC Characterisation Service and the personnel of the National EPSRC XPS User's Service (NEXUS) for the XPS analysis. P. S. S. gratefully acknowledges financial support from the Spanish Ministry of Economy and Competitively (MINECO) for the grant MAT2014-59674-JIN, and for a 'Ramón y Cajal' Senior Research Fellowship. The Spanish Scientific Research Council, CSIC (i-LINK+0636) is also acknowledged. A. M. G. gratefully acknowledges financial support from the Wild Fund Scholarship and an STMS grant awarded by the EUBIS COST Action.

References

1 E. Frackowiak and F. Beguin, *Carbon*, 2001, **39**, 937–950.
2 J. R. Miller and P. Simon, *Science*, 2008, **321**, 651–652.
3 M. Kunowsky, A. Garcia-Gomez, V. Barranco, J. M. Rojo, J. Ibañez, J. D. Carruthers and A. Linares-Solano, *Carbon*, 2014, **68**, 553–562.
4 C. D. Gilmore, 2013.
5 W. Kim, H. Oh, Y. Kwak, K. Park, B. K. Ju and K. Kim, *Sensors*, 2015, **15**, 28732–28741.
6 L. L. Zhang and X. S. Zhao, *Chem. Soc. Rev.*, 2009, **38**, 2520–2531.
7 M. Rose, Y. Korenblit, E. Kockrick, L. Borchardt, M. Oschatz, S. Kaskel and G. Yushin, *Small*, 2011, **7**, 1108–1117.
8 T. Kim, H. C. Kang, T. Tran Thanh, J. D. Lee, H. Kim, W. S. Yang, H. G. Yoon and K. S. Suh, *RSC Adv.*, 2012, **2**, 8808–8812.
9 C. Zhao and W. Zheng, *Frontiers in Energy Research*, 2015, **3**.
10 A. G. Pandolfo and A. F. Hollenkamp, *J. Power Sources*, 2006, **157**, 11–27.
11 E. Lim, C. Jo and J. Lee, *Nanoscale*, 2016, **8**, 7827–7833.
12 L. Zhang, F. Zhang, X. Yang, G. K. Long, Y. P. Wu, T. F. Zhang, K. Leng, Y. Huang, Y. F. Ma, A. Yu and Y. S. Chen, *Sci. Rep.*, 2013, **3**.
13 R. Ryoo, S. H. Joo and S. Jun, *J. Phys. Chem. B*, 1999, **103**, 7743–7746.
14 J. H. Knox and P. Ross, *Adv. Chromatogr.*, 1997, **37**, 73–119.
15 K. V. Kumar, S. Gadipelli, K. Preuss, H. Porwal, T. T. Zhao, Z. X. Guo and M. M. Titirici, *ChemSusChem*, 2017, **10**, 199–209.
16 M.-M. Titirici, R. J. White, N. Brun, V. L. Budarin, D. S. Su, F. del Monte, J. H. Clark and M. J. MacLachlan, *Chem. Soc. Rev.*, 2015, **44**, 250–290.
17 P. S. Shuttleworth, V. Budarin, R. J. White, V. M. Gun'ko, R. Luque and J. H. Clark, *Chem.–Eur. J.*, 2013, **19**, 9351–9357.
18 R. J. White, P. S. Shuttleworth, V. L. Budarin, M. De Bruyn, A. Fischer and J. H. Clark, *ChemSusChem*, 2016, **9**, 280–288.
19 P. S. Shuttleworth, J. H. Clark, R. Mantle and N. Stansfield, *Green Chem.*, 2010, **12**, 798–803.
20 A. Borisova, M. De Bruyn, V. L. Budarin, P. S. Shuttleworth, J. R. Dodson, M. L. Segatto and J. H. Clark, *Macromol. Rapid Commun.*, 2015, **36**, 774–779.
21 J. Sánchez-González, F. Stoeckli and T. A. Centeno, *J. Electroanal. Chem.*, 2011, **657**, 176–180.
22 Y.-R. Rhim, D. Zhang, D. H. Fairbrother, K. A. Wepasnick, K. J. Livi, R. J. Bodnar and D. C. Nagle, *Carbon*, 2010, **48**, 1012–1024.
23 H. L. Parker, A. J. Hunt, V. L. Budarin, P. S. Shuttleworth, K. L. Miller and J. H. Clark, *RSC Adv.*, 2012, **2**, 8992–8997.
24 Q. Wang, J. Yan and Z. J. Fan, *Energy Environ. Sci.*, 2016, **9**, 729–762.
25 H. X. Ji, X. Zhao, Z. H. Qiao, J. Jung, Y. W. Zhu, Y. L. Lu, L. L. Zhang, A. H. MacDonald and R. S. Ruoff, *Nat. Commun.*, 2014, **5**.
26 Z. Li, Z. Xu, H. Wang, J. Ding, B. Zahiri, C. M. B. Holt, X. Tan and D. Mitlin, *Energy Environ. Sci.*, 2014, **7**, 1708–1718.
27 M.-Q. Zhao, C. E. Ren, Z. Ling, M. R. Lukatskaya, C. Zhang, K. L. Van Aken, M. W. Barsoum and Y. Gogotsi, *Adv. Mater.*, 2015, **27**, 339–345.
28 J. Hu, Z. Kang, F. Li and X. Huang, *Carbon*, 2014, **67**, 221–229.
29 X. Y. Meng, Q. Cao, L. Jin, X. H. Zhang, S. L. Gong and P. Li, *J. Mater. Sci.*, 2017, **52**, 760–769.
30 G. C. Pradhan and S. K. Swain, *Polym. Compos.*, 2016, **37**, 2083–2091.
31 N. Deprez and D. S. McLachlan, *J. Phys. D: Appl. Phys.*, 1988, **21**, 101–107.
32 V. M. A. Calado and A. Ramos, *Starch-based blends, composites and nanocomposites*, RSC, Cambridge, CB4 0WF, UK, 2016.
33 H. J. Salavagione, J. Sherwood, M. De bruyn, V. L. Budarin, G. J. Ellis, J. H. Clark and P. S. Shuttleworth, *Green Chem.*, 2017, **19**, 2550–2560.
34 P. Sun, S. Kuga, M. Wu and Y. Huang, *Cellulose*, 2014, **21**, 2469–2478.
35 K. S. W. Sing, D. H. Everett, R. A. W. Haul, L. Moscou, R. A. Pierotti, J. Rouquerol and T. Siemieniewsja, *Pure Appl. Chem.*, 1985, **57**, 603–619.
36 Y. Gogotsi and P. Simon, *Science*, 2011, **334**, 917–918.
37 J. Gamby, P. L. Taberna, P. Simon, J. F. Fauvarque and M. Chesneau, *J. Power Sources*, 2001, **101**, 109–116.
38 P. S. Shuttleworth, V. Budarin and J. H. Clark, *J. Therm. Anal. Calorim.*, 2011, **105**, 577–581.
39 H. J. Salavagione, J. Sherwood, M. De bruyn, V. L. Budarin, G. J. Ellis, J. H. Clark and P. S. Shuttleworth, *Green Chem.*, 2017, DOI: 10.1039/c7gc00112f.
40 P. S. Shuttleworth, V. Budarin and J. H. Clark, *J. Mater. Chem.*, 2009, **19**, 8589–8593.
41 E. Desimoni, G. I. Casella, A. Morone and A. M. Salvi, *Surf. Interface Anal.*, 1990, **15**, 627–634.
42 A. Bellunato, H. Arjmandi Tash, Y. Cesa and G. F. Schneider, *ChemPhysChem*, 2016, **17**, 785–801.
43 S. Fujii and T. Enoki, *Acc. Chem. Res.*, 2013, **46**, 2202–2210.
44 L. A. J. Garvie, A. J. Craven and R. Brydson, *Am. Mineral.*, 1994, **79**, 411–425.